

# Measuring the Stellar-to-Halo Mass Relation at $\sim 10^{10}$ Solar masses, using space-based imaging of galaxy-galaxy strong lenses

Kaihao Wang<sup>1,2,3</sup>, Xiaoyue Cao<sup>3,1\*</sup>, Ran Li<sup>2,3</sup>, James W. Nightingale<sup>4,5,6</sup>, Qiuhan He<sup>5</sup>, Aristeidis Amvrosiadis<sup>5</sup>, Richard Massey<sup>5,6</sup>, Maximilian von Wietersheim-Kramsta<sup>5,6</sup>, Leo W.H. Fung<sup>5,6</sup>, Carlos S. Frenk<sup>5</sup>, Shaun Cole<sup>5</sup>, Andrew Robertson<sup>7</sup>, Samuel C. Lange<sup>5</sup>, Xianghao Ma<sup>1,2,3</sup>

<sup>1</sup> National Astronomical Observatories, Chinese Academy of Sciences, 20A Datun Road, Chaoyang District, Beijing 100012, China

<sup>2</sup> School of Physics and Astronomy, Beijing Normal University, Beijing 100875, China

<sup>3</sup> School of Astronomy and Space Science, University of Chinese Academy of Sciences, Beijing 100049, China

<sup>4</sup> School of Mathematics, Statistics and Physics, Newcastle University, Newcastle upon Tyne, NE1 7RU, UK

<sup>5</sup> Institute for Computational Cosmology, Department of Physics, Durham University, South Road, Durham DH1 3LE, UK

<sup>6</sup> Centre for Extragalactic Astronomy, Department of Physics, Durham University, South Road, Durham DH1 3LE, UK

<sup>7</sup> Observatories, Carnegie Institution for Science, 813 Santa Barbara Street, Pasadena, CA 91101, USA

Accepted XXX. Received YYY; in original form ZZZ

## ABSTRACT

The stellar-to-halo mass relation (SHMR) embodies the joint evolution of galaxies and their host dark matter halos. However, the relation is poorly constrained at sub-galactic masses, because the stellar emission from such objects is so faint. However, it is possible to directly detect the *mass* of halos along the line of sight to a strong gravitational lens, when they perturb one of its multiple images. Space telescopes including Euclid, CSST, and Roman will soon discover millions of galaxy-galaxy strong lensing systems. We simulate Euclid-like imaging of a typical lens galaxy, and find that a lensing reconstruction is sensitive to  $3 \times 10^{10}$  subhalos with various positions and concentrations, at statistical significance  $> 3.6\sigma$ . The subhalo mass can be measured without bias, provided the model simultaneously fits light from both the main lens and the subhalo. A future sample of 48 subhalos with  $\geq 5\sigma$  detection significance would constrain the SHMR at this mass range with  $1\sigma$  uncertainty of 0.045 dex: distinguishing between different theoretical predictions at the sub-galactic scale. Follow-up spectroscopy is needed to measure lens and source redshifts; follow-up imaging at greater spatial resolution and depth would substantially improve the measurement, and eliminate false-positives at even lower halo masses.

**Key words:** dark matter – gravitational lensing: strong – galaxies: evolution

## 1 INTRODUCTION

In the framework of standard cosmology, galaxies are thought to form within cold dark matter (CDM) halos. Initially, dark matter is distributed in small halos, which grow over time through accretion and merging processes, evolving into the larger halos (Frenk & White 2012). Gas collapses within the dominant gravitational potential wells of these dark matter halos, leading to a galaxy forming at their centers. Although galaxy formation and evolution involves complex physical processes, the properties of galaxies are widely believed to correlate with those of their host dark matter halos. A well-known example of this correlation is the stellar-to-halo mass relation (SHMR), which links the stellar mass of galaxies to the mass of their host halos. Various methods have been developed to evaluate this relation. For instance, abundance matching (AM; e.g., Behroozi et al. 2010, Moster et al. 2012, Girelli et al. 2020) assumes a monotonic relationship between stellar mass and halo mass, whereby more

massive halos host more massive galaxies, thus establishing a connection between the stellar mass function and the halo mass function. Alternatively, semi-analytic galaxy formation models can be applied to match halo populations to observed stellar populations (Mitchell et al. 2015). Simulations also provide predictions of the SHMR at specific mass scales (e.g., Niemiec et al. 2019, 2022; Engler et al. 2020; Sifón & Han 2024). However, current SHMR estimates often lack robust constraints for halos with masses  $\lesssim 10^{10} M_{\odot}$ , and there is significant scatter across different studies (see Figure 9 of Girelli et al. 2020). A primary source of this uncertainty stems from the incompleteness of galaxy catalogs at lower stellar mass scales ( $\lesssim 10^8 M_{\odot}$ ), as low-mass galaxies are challenging to observe due to their low surface brightness. Additionally, simulations at these small mass scales are often hindered by limited resolution, making it difficult to produce reliable halo catalogs.

Strong gravitational lensing provides an effective method to address this challenge. When light from a distant source passes near a massive foreground galaxy, it is deflected by the gravitational potential of both the galaxy and its surrounding halo. This deflection

\* E-mail: xycao@nao.cas.cn

distorts the image, producing characteristic ring- or arc-like structures. As this process depends solely on the mass distribution of the foreground lensing galaxy, fitting the lensed image with appropriate mass and light models enables us to measure the lens galaxy's mass. Moreover, if a subhalo perturbs the image, its influence can be characterized by incorporating an additional mass model representing it, allowing us to probe the subhalo's properties (Vegetti et al. 2010, 2012, 2014; Ritondale et al. 2019b; He et al. 2022a; Nightingale et al. 2023; Lange et al. 2024), and test the structure formation model of  $\Lambda$ CDM (e.g. Li et al. 2016, 2017; Ritondale et al. 2019a; Minor et al. 2021; Amorisco et al. 2021; He et al. 2022b; Despali et al. 2024). In recent decades, the detection of subhalos through strong lensing has been constrained by the absence of sky surveys that are simultaneously wide, deep, and high-resolution, key characteristics required to produce sufficient lens samples for large-scale subhalo searches (e.g. Vegetti et al. 2014). However, advancements in next-generation space telescopes, including the JWST, Euclid (Euclid Collaboration et al. 2024), the upcoming CSST (Zhan 2021), and the Roman (Spergel et al. 2015), are expected to overcome this limitation. For example, O'Riordan et al. (2023) predicts that Euclid will detect approximately 2,500 new subhalos. Since the CSST offers comparable depth, resolution, and sky coverage to Euclid (Cao et al. 2023), it is expected to achieve a similar level of subhalo detections, with the added benefit of providing optical color information, which is crucial for verifying the reliability of subhalo identification. These advancements will greatly expand strong lensing samples and enable more comprehensive statistical analyses. By constructing a subhalo catalog through strong lensing studies, including the possible detection of satellite galaxies within these subhalos, we can place tighter constraints on the SHMR at smaller scales.

While previous studies have demonstrated the ability to unbiasedly model the mass of  $\sim 10^9 M_\odot$  subhalos in Hubble Space Telescope (HST) observations (Vegetti & Koopmans 2009; He et al. 2023), the feasibility of achieving unbiased mass estimates with lower-resolution data from upcoming surveys like Euclid and CSST remains an open question. Given the expected detection of thousands of subhalos by these surveys, understanding the accuracy of mass modeling is crucial. Furthermore, the influence of subhalo properties on mass estimation needs investigation. For instance, highly concentrated subhalos can produce similar perturbations to more massive, moderately concentrated ones, potentially enhancing the detection signal (Amorisco et al. 2022). Additionally, subhalos with dark matter masses around  $\sim 10^{10} M_\odot$  often host satellite galaxies. While standard subhalo mass-halo mass relations (SHMR) predict those halos have a galaxy with a stellar mass of  $\sim 10^8 M_\odot$  or lower, the galaxy's mass and light contributions could introduce additional systematic errors if not properly accounted for.

To investigate the constraints on the SHMR using subhalos in galaxy-galaxy strong lenses, in this work, we assess the accuracy with which the masses of subhalos with  $M_{200} \sim 10^{10} M_\odot$  can be determined. This mass range lies within the detection limits of upcoming surveys such as Euclid and CSST. As a proof-of-concept, we assume a fiducial subhalo mass of  $M_{200} = 3 \times 10^{10} M_\odot$  and systematically vary intrinsic subhalo properties, including concentration and position. Additionally, we incorporate a galaxy light component to analyze its impact on the accuracy of subhalo mass measurements. Mock images are generated based on the specifications of the Visible Camera (VIS) on Euclid. Since the CSST offers image quality comparable to Euclid VIS, the main results of this study are expected to be transferable to CSST observations. For simplicity, the redshifts of the main lens and subhalo are fixed at  $z = 0.2$ , while the source redshift is set at  $z = 1.0$ .

The structure of this paper is as follows: In Section 2, we describe the mock simulations and fitting procedures. Section 3 presents our lens modelling results. In Section 4, we discuss our mass measurement results and consider prospects for future applications. We summarize our findings in Section 5. We adopt the cosmological parameters from Planck 2015 (Ade et al. 2016) throughout the work.

## 2 METHOD

For this proof-of-concept study, we simplify our analysis by focusing on a single ring-like lensing configuration<sup>1</sup> and assuming a single subhalo with a mass of  $\sim 10^{10.5} M_\odot$  within the lens galaxy. We vary the subhalo position and concentration to investigate whether the mass of a subhalo can be accurately recovered through strong lensing. Additionally, we include a mass or light component to represent the potential presence of a satellite galaxy hosted by the subhalo. This allows us to evaluate whether these satellite signals introduce contamination into lensing analyses and contribute additional systematic errors to our modeling. Next, we generate a catalog of detected subhalos, stack their inferred masses, and assess the extent to which the SHMR can be constrained using these systems. All mock images are generated to emulate Euclid VIS observations, reflecting the capabilities of next-generation space surveys. This section describes the models used for image simulation and the pipelines employed for image modeling. All simulations and fitting processes are performed using the open-source software PyAutoLens (Nightingale & Dye 2015; Nightingale et al. 2018, 2021).

### 2.1 Image Simulation

Figure 1 presents our baseline lensing image, consisting of a mass model for the main lens and a light model for the background source. This lensing simulation without a subhalo is referred to as the 'macro model'. All subsequent mock lensing simulations, which include a subhalo and associated lens modeling analyses, are based on this image.

#### 2.1.1 Macro Model

We use a power-law mass model for the main lens (Tessore & Metcalf 2015). Following Nightingale et al. (2023), the convergence is given by:

$$\kappa(\xi) = \frac{3 - \gamma}{1 + q} \left( \frac{R_E}{\xi} \right)^{\gamma - 1}, \quad (1)$$

where  $\gamma$  is the density slope,  $R_E$  is Einstein radius, and  $\xi = \sqrt{x^2 + y^2/q^2}$  is the elliptical radius from centre. In PyAutoLens

<sup>1</sup> As demonstrated by (Despali et al. 2022; O'Riordan et al. 2023), lenses with ring-like morphologies generally provide higher sensitivity for subhalo detection. Consequently, it is expected that most "golden lens" samples identified in future surveys, such as Euclid and CSST, which enable accurate subhalo detection, will exhibit ring-like structures. Thus, our fiducial lensing image serves as a representative morphology for evaluating the accuracy of subhalo detection. Space-based imaging surveys like CSST and Euclid are anticipated to discover tens of thousands of ring-like lenses (e.g. Cao et al. 2023), making the exploration conducted in this work both realistic and most relevant for future studies.

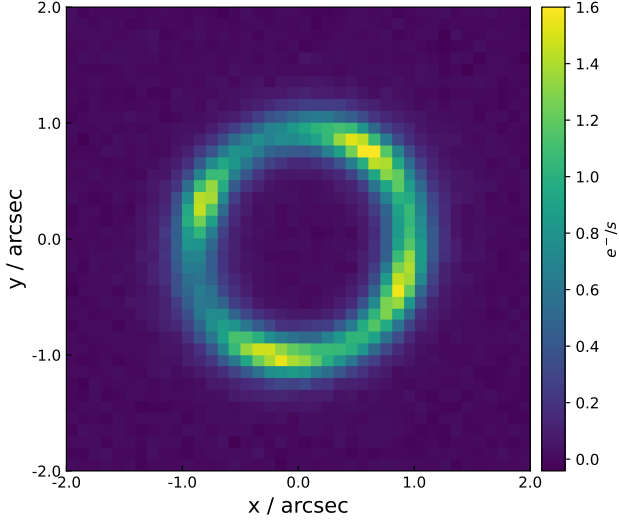


**Figure 1.** The simulated mock image based on the macro model. The parameter values used for this simulation are listed in Table 1. The image has a pixel size of  $0.1''$  and is convolved with a Gaussian PSF with a FWHM of  $0.18''$

the axis ratio  $q$  and the position angle  $\phi$  are reparameterized as two components:

$$e_1 = \frac{1-q}{1+q} \sin 2\phi, \quad e_2 = \frac{1-q}{1+q} \cos 2\phi. \quad (2)$$

While external shear is not included in the simulation of mock images, it is incorporated during the lens modeling process. This is because external shear is a standard component in real lens modeling, accounting for line-of-sight effects, nearby perturbations, and unmodeled angular complexities in the main lens mass distribution (Cao et al. 2022; Etherington et al. 2024). The cored Sérsic profile (Graham et al. 2003) is used to describe the brightness distribution of the background source, defined as

$$I(\xi) = I' \left( 1 + \left( \frac{r_b}{\xi} \right)^\alpha \right)^{\frac{\gamma}{\alpha}} \exp \left[ -b_n \cdot \left( \frac{\xi^\alpha + r_b^\alpha}{r_e^\alpha} \right)^{\frac{1}{\alpha n}} \right], \quad (3)$$

where  $I'$  is the scaled intensity factor,  $r_b$  is the break radius separating the inner power-law and outer Sérsic profile,  $\alpha$  controls the transition from the inner to outer profile,  $\gamma$  is the power-law density slope,  $n$  is the Sérsic index,  $b_n$  is a constant determined by  $n$ , and  $r_e$  is the effective radius of the Sérsic profile. The radius  $r$  is measured from the center, and for an elliptical profile, it is defined as  $r = \sqrt{qx^2 + y^2/q}$ . Although a core-Sérsic profile may be too simplistic to capture the complex morphology of a real source galaxy, it is sufficient to access the measurement accuracy of subhalo properties using strong lensing.

### 2.1.2 Subhalo and Associated Galaxy

We adopt the Navarro-Frenk-White (NFW) mass profile (Navarro et al. 1996) for subhalo:

$$\rho(r) = \frac{\rho_0}{(r/R_s)(1+r/R_s)^2}. \quad (4)$$

In PyAutoLens,  $M_{200}$  and concentration are utilized as inputs to compute  $\rho_0$  and  $R_s$ . Here,  $M_{200}$  is defined as the total mass enclosed within a radius,  $r_{200}$ , where the average enclosed mass density is 200

times the cosmic average density. In this work, the  $M_{200}$  is set to  $3 \times 10^{10} M_{\odot}$ . The concentration parameter is given by  $c = r_{200}/R_s$ . Research indicates that the density profile of a dark matter halo follows a specific relation as a function of its total mass and redshift, known as the ‘mass-concentration-redshift relation’ (e.g. Duffy et al. 2008; Ludlow et al. 2016). Wang et al. (2020) used a wide-ranging hierarchical simulation to show that the scatter in halo concentration at a given mass is nearly independent of the halo mass, with a value of approximately 0.15 dex. Throughout the work, we use the mass-concentration relation given by Ludlow et al. (2016) (hereafter L16 relation), as it shows the greatest consistency to recent simulations in the very low-mass regime (Wang et al. 2020). The scatter,  $s_c$  deviating from the median value of L16 relation is used as a model parameter controlling the concentration of the subhalo, which is defined as:

$$s_c \equiv \delta \log c / \sigma_{\log c} = (\log_{10} c - \log_{10} c(M, z)) / \sigma_{\log_{10} c}, \quad (5)$$

where  $\sigma_{\log_{10} c} = 0.15$ . The default  $s_c$  value is 0, except for the samples used to analyze the effect of halo concentration, where we will vary this parameter to simulate subhalos with different concentrations.

A  $10^{10} M_{\odot}$  subhalo is likely to host a dwarf galaxy. Different studies and simulations predict varying galaxy stellar mass ranges for a given subhalo mass, but approximately, a  $10^{10} M_{\odot}$  subhalo can host a satellite galaxy with a total stellar mass of  $\sim 10^8 M_{\odot}$  or less (Girelli et al. 2020). In this study, to perform a conservative analysis, we assume that the relation between stellar mass and halo mass follows Girelli et al. (2020), so that the stellar mass is thereby  $10^{8.22} M_{\odot}$ , which is larger than most predictions. Following Ballard et al. (2024), we assume the stellar mass-to-light ratio is  $2M_{\odot}/L_{\odot}$ , which gives an absolute magnitude of -15.19 (equivalent to an apparent magnitude of 24.83 at  $z = 0.2$ ). The additional galaxy component hosted by the subhalo is included in the mock datasets only to evaluate its contamination effect on lens modelling. Specifically, a Sérsic mass or light component is added at the centre of the subhalo to independently analyse the influence of stellar mass or light. In all other cases, only an NFW mass component is used.

### 2.1.3 Instrument information and data quality

Our mock images are assumed to be observed using the Euclid VIS instrument (Collaboration et al. 2024), which has a pixel size of  $0.1''$ . A Gaussian point spread function (PSF) with a full width at half maximum (FWHM) of  $0.18''$  is applied. In the Euclid survey, half of the sky is observed in four exposures, while the remaining area is covered by three exposures. Each exposure has an integration time of 565 seconds. In this work, we consider only three exposures, resulting in a total exposure time of  $3 \times 565 = 1695$  seconds. For the Euclid VIS instrument, a magnitude zero point of 25.23 (in electrons; Martinet et al. 2019) is used. Combined with a sky background surface brightness of  $22.2 \text{ mag/arcsec}^2$  (Collett 2015), this corresponds to a flux of  $0.1629 \text{ e}^- \text{ s}^{-1} \text{ pixel}^{-1}$ . The readout noise of the Euclid VIS instrument is  $< 4.5 \text{ e}^-$ , which is negligible compared to other noise sources and is therefore excluded from this analysis. The apparent magnitude of the source before lensing is assumed to be 26.84, a representative value for the galaxy-galaxy strong lensing catalogue produced by Collett (2015). This results in a maximum signal-to-noise ratio (SNR) of approximately 50 in the lensed images. Table 1 summarises the model parameters used in this simulation.

## 2.2 Adaptive Source Reconstruction

For a given set of mass model parameters, the lensed source emission is ray-traced back to the source plane and reconstructed onto an adap-

**Table 1.** Parameters used to simulate mock images.

	values
<b>Input lens mass</b>	
<b>model name</b>	<b>elliptical power-law</b>
centre (x, y) [(" , ")]	(-0.0012, -0.0342)
axis ratio	0.7
position angle [°]	156.6
Einstein radius ["]	1.0
slope	2.16
redshift	0.2
mass within Einstein radius [ $M_{\odot}$ ]	$1.35 \times 10^{11}$
<b>Input subhalo mass</b>	
<b>model name</b>	<b>NFW</b>
$M_{200}$ [ $M_{\odot}$ ]	$3 \times 10^{10}$
redshift	0.2
<b>Input satellite galaxy (if added)</b>	
<b>model name</b>	<b>spherical Sérsic</b>
intensity (light) [ $e^{-} s^{-1} pixel^{-1}$ ]	$7.35 \times 10^{-3}$
intensity (mass) [ $\kappa$ ]	$2.33 \times 10^{-3}$
$r_e$ ["]	0.38
Sérsic index	1.3
<b>Input Source light</b>	
<b>model name</b>	<b>core Sérsic</b>
intensity at $r_b$ [ $e^{-} s^{-1} pixel^{-1}$ ]	1.919
centre (x, y) [(" , ")]	(0.03, -0.05)
$(e_1, e_2)$	(0.073, 0.061)
$r_e$ ["]	0.18
$r_b$ ["]	0.05
Sérsic index	1.7
$\alpha$	2.0
$\gamma$	0.0
redshift	1.0

tive mesh. Following the formalism of [Nightingale et al. \(2023\)](#), we model the source using a Voronoi mesh with natural neighbor interpolation ([Sibson 1981](#)) and apply adaptive regularization to smooth the reconstruction based on the source luminosity at each point<sup>2</sup>. The likelihood function for these fits follows [Suyu et al. \(2006\)](#) and is provided in equation 17 of [Nightingale et al. \(2023\)](#). Appendix A of [He et al. \(2024\)](#) also illustrates the Voronoi natural neighbor interpolation scheme and adaptive regularization in detail.

A key step in the source analysis is defining the centers of the source pixels. Previous PyAutoLens works have employed two approaches. The first overlays a rectangular Cartesian grid of shape  $(y_{\text{pix}}, x_{\text{pix}})$  over the image plane, retaining all coordinates within the mask and tracing them to the source plane via the mass model. The second uses a weighted KMeans clustering algorithm ([Pedregosa et al. 2011](#)) to distribute image-plane coordinates such that they cluster around the brightest regions of the lensed source galaxy. The first method adapts to the *lens mass model magnification*, while the second adapts to the *lensed source emission*. However, KMeans cannot assign more than one source pixel per image pixel, limiting reconstruction resolution and potentially introducing bias, particularly for lower-resolution Eu-

clid images. A straightforward solution is to apply KMeans to an over-sampled image (e.g., dividing each image pixel into  $11 \times 11$  sub-pixels), allowing multiple source pixels to cluster within one image pixel (e.g. [Minor 2024](#)). However, it is time-consuming to apply the KMeans algorithm directly to such a large 2D array. Instead, we convert the 2D over-sampled grid into a 1D array using a Hilbert space-filling curve ([Hilbert 1891](#)) and allocate source pixels along the 1D grid based on the lensed source flux distribution (e.g., the best reconstruction from the previous fitting phase). Brighter regions receive more source pixels, and clustering strength can be controlled by rescaling the lensed source flux distribution. The new clustering scheme is named `HilbertMesh` in PyAutoLens and the detailed description will be found in [He et al. in prep. \(2025\)](#).

### 2.3 Fitting procedure

We use the SLAM pipelines implemented in PyAutoLens to model the lensing images (see also [Etherington et al. 2022](#); [Cao et al. 2022](#); [He et al. 2023](#); [Nightingale et al. 2023](#)). These pipelines employ a non-linear search chaining method, which breaks a high-dimensional, complex parameter space into a series of simpler, more manageable searches. Initial searches use simplified models and explore less complex parameter spaces, establishing priors for subsequent, more detailed searches. This ensures that the final, comprehensive search begins near the global maximum. This sequential approach improves the efficiency of the sampling process and reduces the risk of missing the global best solutions. In this work, we do not simulate lens light, so no lens light model is included in the fit. During the fitting procedure, non-linear searches are performed using the neural network-based sampler `Nautilus` ([Lange 2023](#)). This sampler uses nested sampling, which returns Bayesian evidence essential for subhalo detection. Although we simulate mock lenses with a parametric core-Sérsic source—indicating that parametric sources are sufficient for lens modelling—we employ a pixelised source model. This approach is necessary for modelling real lenses, which often feature complex morphologies. The full subhalo modelling pipelines are as follows:

(a) **Source Parametric Pipeline:** A simple parametric model is first used to fit the lensing image, providing a rapid initial estimate of the lens mass parameters. The lens mass distribution is parameterised by a Singular Isothermal Ellipsoid (SIE) profile with external shear, while the source light is modelled using a core-Sérsic profile.

(b) **Source Pixelised Pipeline:** To reconstruct the complex structure of the background source, we adopt the Voronoi mesh source model. This step involves two consecutive fits. In the initial fit, the Voronoi mesh centres are determined by overlaying a Cartesian grid on the image plane. The mass model is an SIE profile with external shear, with all parameters allowed to vary and priors informed by the results of step (a). In the second fit, the lens mass parameters are fixed, and only the source pixelisation parameters are optimised. The Voronoi mesh centres are then determined using the Hilbert sampling technique (see Section 2.2), enabling the source pixels to better reconstruct the unlensed source morphology. Most pixels reconstruct the brightest regions of the lensed arc, while an appropriate proportion reconstructs the background regions.

(c) **Mass Pipeline:** After determining the optimal pixelisation scheme for the source light, we employ a more advanced mass model, parameterised as an elliptical power-law profile with external shear.

(d) **Subhalo Pipeline:** We perform a model comparison to determine whether a lens model with a subhalo is preferred over a lens model without a subhalo, thereby indicating the detection of a subhalo. This model comparison is based on the Bayesian evidence of

<sup>2</sup> In PyAutoLens, these schemes correspond to the `VoronoiNNBrightnessImage` pixelization and the `AdaptiveBrightnessSplit` regularization.

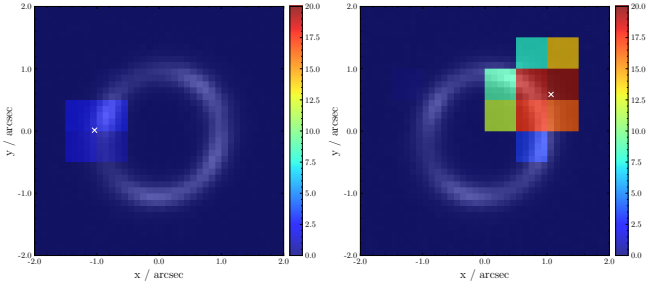


**Figure 2.** Evidence increasing maps illustrating an undetected (left) and a detected (right) subhalo. The white cross marks the input subhalo position. The colour scale represents the increase in logarithmic evidence,  $\Delta \ln E$ , when a subhalo is included in each  $0.5'' \times 0.5''$  grid cell. In the left panel, no grid cell has a  $\Delta \ln E > 5$ , and thus no subhalo detection is claimed. In the right panel, the grid cell with the highest  $\Delta \ln E = 19.55$  is identified as the most probable location of a subhalo. This conclusion requires further validation using a refined subhalo model, in which the prior on the subhalo position is relaxed (i.e., not restricted to individual grid cells).

each model. First, we estimate the Bayesian evidence of the model without a subhalo by fitting the image with models identical to those used in the mass pipeline, with priors also based on the results of the mass pipeline. For the model with a subhalo, given the complex parameter space and the subtle nature of subhalo perturbations, directly sampling the parameters is inefficient and unreliable. Instead, we divide the entire lensing image area into a  $5 \times 5$  grid of cells. In each grid cell, we perform a lensing model fit, including a subhalo and assuming the subhalo’s position is uniformly distributed within that cell. We then summarize the lens modeling results from all grid cells. The model fit with the highest Bayesian evidence should provide the best estimate of the subhalo’s position. Next, we perform a refined model fit, where we set a Gaussian prior for the subhalo position centered on the previous best estimate, with a standard deviation of  $0.5''$ . The  $M_{200}$  is assigned a log-uniform prior from  $10^6 M_{\odot}$  to  $10^{11} M_{\odot}$ . This fit provides the final Bayesian evidence for the model with a subhalo. If a subhalo is present, a significant increase in Bayesian evidence is expected compared to the no-subhalo model. According to Jeffreys’ scale (Jeffreys 1998), fits with  $\Delta \ln E \geq 5$  are classified as detections, where  $\Delta \ln E$  represents the increase in the logarithm of Bayesian evidence from the no-subhalo model to the subhalo-included model, and  $\Delta \ln E = 5$  corresponds to a significance of  $3.6\sigma$ .

In Figure 2, we present evidence increase maps for two mock lensing images as examples to illustrate the detection of a subhalo. Each system contains an input subhalo, marked with white crosses. The colours represent the  $\Delta \ln E$  values when a subhalo is included in each  $0.5'' \times 0.5''$  grid cell. In the left panel, no grid cell has a  $\Delta \ln E > 5$ , and thus no subhalo detection is claimed for this lensing image. In the right panel, the grid cell with the highest  $\Delta \ln E$  has a value of approximately 19.6, which is significantly above the detection threshold. Therefore, we claim a possible detection of a subhalo in this lensing image. This conclusion must be further validated using the refined subhalo model, where the prior on the subhalo position is relaxed (not confined to individual grid cells), and more accurate Bayesian evidence is obtained through a more thorough sampling configuration. Generally, we find that the logarithmic Bayesian evidence of the final refined subhalo model is consistent with that of the subhalo model from the grid search step, with the difference being less than one.

### 3 RESULTS

We present our results on the accuracy with which the properties of  $\sim 10^{10} M_{\odot}$  subhalos can be measured using galaxy-galaxy strong lensing data from upcoming Euclid observations. Sections 3.1 to 3.2 describe how various subhalo properties, such as position and concentration, and the effects of contamination from a satellite galaxy hosted by the subhalo, influence the measurement of the subhalo properties. Additionally, we evaluate the extent to which these subhalo measurements can constrain the subhalo mass–stellar mass relation (SHMR), as discussed in Section 3.3.

#### 3.1 Measuring subhalo properties

We simulate 161 mock images, each containing a subhalo randomly distributed within an annular mask whose inner and outer radii are  $0.55''$  and  $1.5''$ , respectively. The subhalo mass is fixed at  $3 \times 10^{10} M_{\odot}$ , with its concentration following the L16 relation. After applying the detection criteria outlined in Section 2.3, we obtain 74 detections. To quantify the quality of our fits, we measure the bias in terms of how many  $\sigma$  the posterior overestimates or underestimates  $M_{200}$ . The mass bias of the 74 detected subhalos is shown in Figure 3. The distribution of detected subhalos agrees well with the sensitivity map from O’Riordan et al. (2023), as most detections lie on or near the brightest regions of the lensed arc. We find the subhalo mass can be accurately measured irrespective of the location as long as it is detected according to our detection criteria. Notably, the subhalo mass can be accurately recovered regardless of its location, provided it meets our detection criteria of  $\Delta \ln E > 5$ . To further demonstrate the accuracy of our fitting results, we examine the relationship between mass bias and the increase in Bayesian evidence, as shown in Figure 4. For our detection threshold of  $\Delta \ln E > 5$ , we find no significant correlation between mass bias and Bayesian evidence for the detected subhalos. In most cases,  $M_{200}$  is recovered within  $1\sigma$ . Nevertheless, there are four outliers whose  $M_{200}$  values are underestimated by more than  $2\sigma$ . This discrepancy is likely due to random noise, as indicated by similar outcomes in samples where we keep the subhalo position and mass distribution fixed to their true values, but vary only the noise realisation (see the blue histogram in Figure 6). We therefore conclude that a detection threshold of  $\Delta \ln E > 5$  is generally sufficient to achieve unbiased subhalo mass measurements for Euclid-like lensing data. In Figure 4, we also present results for samples that do not meet our detection threshold but show an increase in the maximum log-likelihood of 10 for the subhalo-included model. These cases can be viewed as *tentative detections* (He et al. 2023). However, they reveal a notable underestimation of their masses and a strong positive correlation between mass bias and Bayesian evidence. This finding emphasises the importance of employing Bayesian evidence-based metrics to define the subhalo detection threshold.

In the real universe, there is intrinsic scatter in the mass–concentration relation of subhalos, raising the possibility of detecting extremely compact or diffuse objects. Do the image quality and depth of Euclid lensing data enable the detection of such outlier subhalos? Can their mass and concentration be measured with sufficient accuracy? These are non-trivial questions, given the significant degeneracy between subhalo mass and concentration in lens modelling. To address these questions, we simulate an image containing an NFW subhalo with a concentration  $2\sigma$  higher than predicted by the L16 relation. By fitting this image, we derive the posterior distribution shown in Figure 5. The banana-shaped contours highlight the degeneracy between  $M_{200}$  and  $\delta \log(c)/\sigma_{\log c}$ ; however, the Euclid-

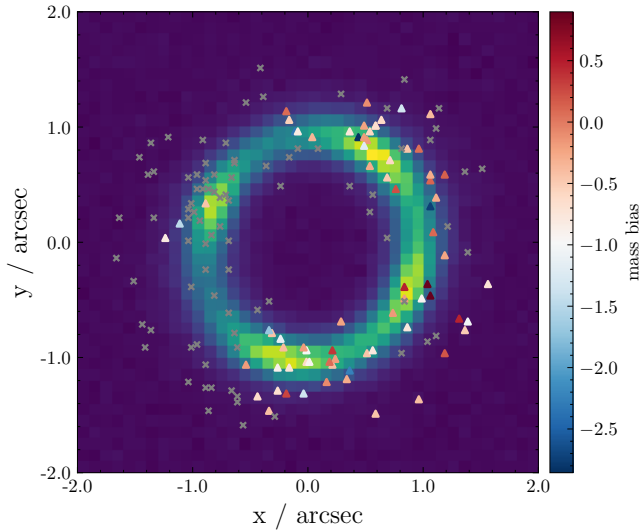


**Figure 3.** Mass modelling biases for mock lenses with an input subhalo at different positions, indicated by grey crosses or triangles. The background image, generated using the macro model, illustrates the overall lensing morphology. Triangles represent locations where the input subhalo is successfully detected via lens modelling, with their colours indicating the mass measurement bias. This mass bias is defined as the difference between the median of the posterior distribution and the true value, expressed in units of the reported statistical uncertainty ( $\sigma$ ). Grey crosses mark subhalo positions where no detection was reported by our modelling pipelines.

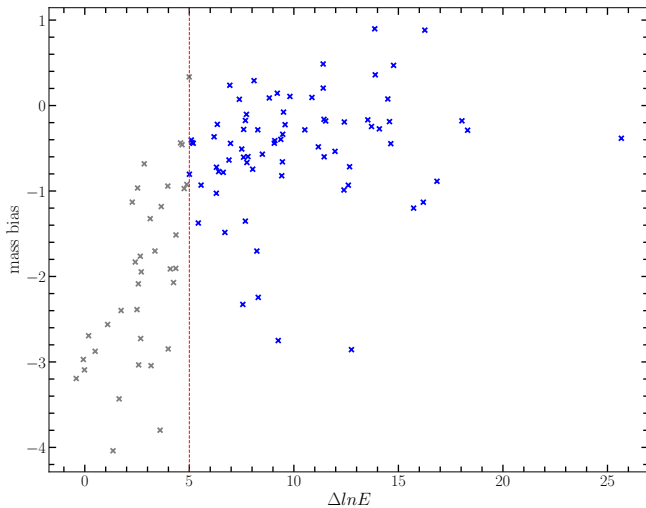


**Figure 4.** Relation between mass modelling bias and the logarithmic evidence increase ( $\Delta \ln E$ ) from the macro model to the subhalo-included model. In addition to detections with  $\Delta \ln E > 5$  (blue crosses), we also show modelling results with  $\Delta \ln \mathcal{L} > 10$ , which may be interpreted as potential detections in certain cases (grey crosses). Under the current detection threshold (red dashed line), no apparent correlation is observed between mass bias and the evidence increase. This suggests that a logarithmic evidence increase of  $\Delta \ln E > 5$  is sufficient to obtain unbiased individual subhalo measurements using Euclid strong lensing data.

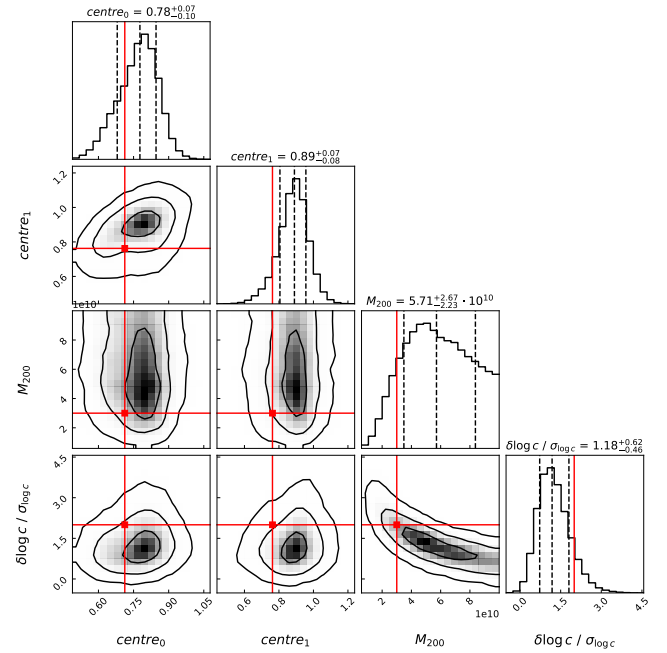


**Figure 5.** The posterior distribution for an example mock lens with an input NFW subhalo whose concentration is  $2\sigma$  above the Ludlow et al. (2016) relation. The input true values are shown by red lines, while the  $1\sigma$  credible intervals are represented by grey dashed lines. The 2D contours correspond to the  $1\sigma$ ,  $2\sigma$ , and  $3\sigma$  credible intervals, respectively. The concentration of the subhalo is treated as a free parameter during lens modelling by directly sampling  $s_c = \delta \log c / \sigma_{\log c}$ , where  $\delta \log c$  is the deviation of the concentration from the Ludlow et al. (2016) relation, and  $\sigma_{\log c} = 0.15$ .

like data are sufficient to constrain both  $M_{200}$  and the concentration to within approximately  $1\sigma$ . We therefore conclude that Euclid-quality data enable not only the detection of such subhalos but also accurate measurements of their mass and concentration<sup>3</sup>.

### 3.2 Systematic bias from satellite galaxies

We investigate whether satellite galaxies hosted by subhalos introduce biases into subhalo measurements in strong lensing analyses. Building on the models detailed in Table 1, we simulate three sets of 100 images, each with the subhalo position fixed at  $x = 0.7625''$  and  $y = 0.7125''$ , while varying only the noise realisation. The first set includes an NFW subhalo as the sole perturber. The second set adds a Sérsic mass component, centred on the NFW subhalo, to represent the stellar mass of its satellite galaxy. The third set incorporates a Sérsic light component, also centred on the NFW subhalo, to represent the satellite galaxy's emission. This approach allows us to assess the sensitivity of subhalo modelling to both mass and light contamination from the satellite galaxy. Figure 6 presents histograms of the resulting mass modelling biases, leading to two key findings.

First, including the stellar mass of subhalos does not significantly affect their mass measurements, resulting in minimal bias when constraining the SHMR using strong lensing. Second, in samples with a light component,  $M_{200}$  is systematically overestimated, with the

<sup>3</sup> The ultra-diffuse subhalo may not be detectable due to its negligible lensing effect.

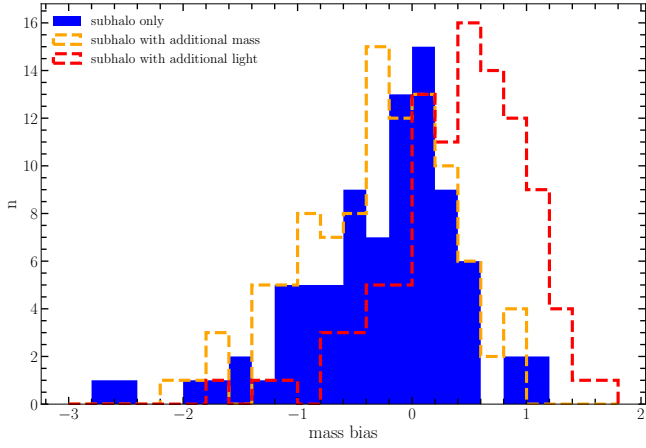


**Figure 6.** Histograms of the mass measurement bias derived from model fits to the mock lensing images are presented. The mass measurement bias is quantified as the number of statistical  $1\sigma$  uncertainties by which the model over- or underestimates the true  $M_{200}$ . Results are shown for three image sets, each with a different input perturber. The first set features a standard  $3 \times 10^{10} M_{\odot}$  NFW subhalo (blue shaded). The second set incorporates an additional Sérsic mass profile centred on the NFW subhalo (orange dashed). The third set includes an additional Sérsic light profile within the NFW subhalo (red dashed). For each dataset, all mock lensing images are simulated with identical model parameters but with different noise realisations.

histogram peaking at approximately  $0.5\sigma$ . This overestimation occurs because some of the additional light is misidentified as part of the lensed arc, amplifying the apparent perturbation. Although each measurement for individual systems remains within  $3\sigma$ , this shift suggests that light contamination from the satellite galaxy can introduce subtle biases when statistically stacking mass measurements from multiple lenses to constrain the SHMR. Conversely, the presence of stellar light provides a measurable signal of the subhalo. While ignoring this emission biases the model fits, incorporating it into the lens model would enable recovery of the stellar light (and thus the stellar mass) of such subhalos in Euclid observations. We refrain from performing this more detailed modelling here for simplicity, but the availability of this information is highly relevant for future lens modelling studies aiming to achieve a more precise determination of subhalo properties.

### 3.3 Constraining stellar-to-halo mass relation

Strong lensing measurements of subhalo masses, combined with stellar mass estimates of their satellite galaxies obtained through independent techniques (e.g. stellar population synthesis modelling), provide a robust method for constraining the stellar-to-halo mass relation (SHMR). Throughout this work, we adopt an NFW profile to describe subhalos and define their mass as  $M_{200}$ . Although a truncated NFW profile more accurately accounts for the mass loss experienced by a subhalo when it merges into a larger host halo, using the untruncated form does not compromise the main conclusions of this study. The NFW model can readily be replaced with the truncated NFW model in future work to achieve a more realistic representation of subhalos in strong lensing analyses.

We adopt the stellar-to-halo mass relation (SHMR) from Girelli et al. (2020) as the fiducial relation for subhalos in our mock lensing simulations. For a subhalo with a mass of  $3 \times 10^{10} M_{\odot}$ , this relation predicts a galaxy with a stellar mass of  $10^{8.22}$ . By applying a de-

tection threshold of  $\Delta \ln E > 10$ , we use 48 subhalos from the 100 mock images described in Section 3.2 (blue-shaded histogram in Figure 6) to constrain the SHMR. We suppose that unbiased stellar mass measurements for the associated satellite galaxies are available, with an accuracy of 0.11 dex. This value reflects the average uncertainty for galaxies with stellar masses between  $10^8 M_{\odot}$  and  $10^{8.5} M_{\odot}$  in GAMA DR4 (Driver et al. 2022; Taylor et al. 2011). Using 48 strong lenses, each with the subhalo and stellar mass measurement accuracies outlined above, we apply the following equations:

$$M = \frac{\sum_i M_i \frac{1}{\sigma_i^2}}{\sum_i \frac{1}{\sigma_i^2}}, \quad \sigma^2 = \frac{1}{\sum_i \frac{1}{\sigma_i^2}}, \quad (6)$$

to stack these measurements. Here,  $M_i$  and  $\sigma_i$  represent the median and  $1\sigma$  uncertainty of the estimated  $M_{200}$  for the  $i^{\text{th}}$  sample. This stacking yields a robust constraint on the subhalo mass, with  $\log M_{200}/M_{\odot} = 10.490 \pm 0.0449$ , as represented by the black cross in Figure 7. This high-precision subhalo mass measurement can be further translated into a strong constraint on the stellar-to-halo mass relation (SHMR), enabling the differentiation of predictions from various works (Behroozi et al. 2010; Moster et al. 2012; Mitchell et al. 2015; Niemiec et al. 2019; Girelli et al. 2020; Shuntov et al. 2022; Sifón & Han 2024; Nelson et al. 2019), as shown by the lines of different colours. Additionally, we observe a biased constraint on the SHMR when the detection threshold is set to  $\Delta \ln E > 5$  (brown cross). This arises because, although the subhalo mass measurement for an individual lens is unbiased, the population-level inference of subhalo mass exhibits bias. This is demonstrated by the negatively skewed Gaussian distribution in Figure 6, where more model fits underestimate  $M_{200}$  than overestimate it. This asymmetry results in a stacked  $\log M_{200}$  of  $10.411 \pm 0.0361$ , which statistically underestimates  $M_{200}$  by  $1.83\sigma$ . We attribute this bias in the population-level subhalo mass measurement to the limited constraining power of the data. Consequently, the posterior distribution of subhalo mass measurements is somewhat influenced by the log-uniform prior assumed during lens modelling, which tends to favour smaller masses. Indeed, increasing the detection threshold to  $\Delta \ln E > 10$  eliminates this biased constraint on the SHMR (black cross), as the lensing data can more robustly constrain the subhalo mass, reducing the influence of the prior.

We also observe that constraints on the SHMR can be biased if the light contribution from the satellite galaxy hosted by the subhalo is not properly accounted for in lens modelling. This is illustrated by the green cross in Figure 7, where the model constraint favours the SHMR prediction of Moster et al. (2012) over the fiducial relation of Girelli et al. (2020). The bias arises because the population-level inference of subhalo mass is skewed (see the red histogram in Figure 6). Our experiments further show that if contamination from a satellite galaxy hosted by a  $10^{10} M_{\odot}$  subhalo biases the lens modelling result, it is more likely caused by the light contribution rather than the mass contribution.

## 4 DISCUSSION

### 4.1 Expectations on constraining the SHMR with strong lensing

Previous investigations of the SHMR (e.g. Behroozi et al. 2010; Moster et al. 2012; Mitchell et al. 2015; Niemiec et al. 2019, 2022) indicate that a subhalo of  $\sim 10^{10} M_{\odot}$  likely hosts a dwarf galaxy whose stellar mass falls between  $10^6$  and  $10^8 M_{\odot}$ . Yet, these galaxies are exceptionally challenging to detect because of their very low

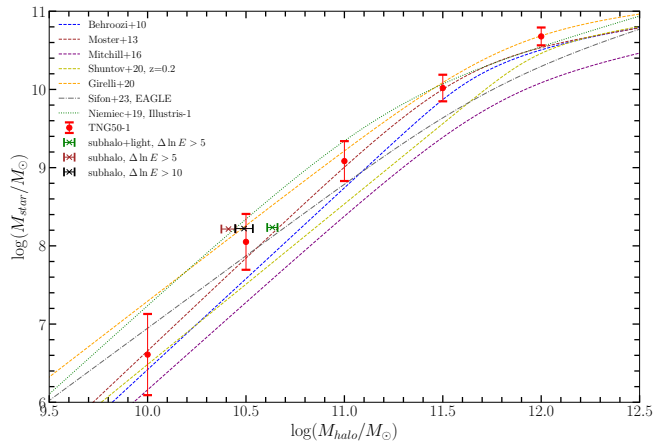


**Figure 7.** Constraining the stellar-to-halo mass relation (SHMR) at  $10^{10} M_{\odot}$  using subhalo mass measurements derived from  $\sim 50$  Euclid mock lenses. The subhalos in the mock lensing data are assumed to follow a fiducial SHMR from [Girelli et al. \(2020\)](#), which corresponds to a stellar mass of  $10^{8.2} M_{\odot}$ . Subhalo mass uncertainties are derived from the lensing analysis, while stellar mass uncertainties are empirically assumed to be  $\sim 10^{-2} M_{\odot}$ , based on results from stellar population synthesis modelling in the GAMA survey. To obtain unbiased population-level subhalo mass measurements, a higher detection threshold of  $\Delta \ln E > 10$  is required, with the corresponding joint constraint on the SHMR indicated by the black marker. In contrast, the default threshold of  $\Delta \ln E > 5$  provides unbiased subhalo mass measurements for individual lenses but is insufficient for accurate population-level mass inference, which is underestimated due to the log-uniform prior assumed in the lensing analysis (brown marker). The light contribution from a potential satellite galaxy residing in the subhalo can significantly overestimate the subhalo mass if not properly accounted for in the lens modelling (green marker). Lines of different colours represent SHMR predictions from previous studies.

surface brightness. Observational surveys thus far have not produced a sufficiently complete catalogue to constrain the SHMR in the  $\sim 10^{10} M_{\odot}$  halo regime. By contrast, strong lensing is sensitive to small perturbations in the lens galaxy, making it feasible to identify many low-mass subhalos. Each subhalo of  $\sim 10^{10} M_{\odot}$  is a potential host of a dwarf galaxy, raising the possibility of discovering numerous dwarf systems in these subhalos. Moreover, strong lensing offers strong constraints on subhalo masses. Our findings show that, with a suitably stringent detection threshold ( $\Delta \ln E > 10$ , equivalent to a  $5\sigma$  significance), one can robustly constrain the SHMR. Hence, strong lensing is poised to become a uniquely powerful method for studying the SHMR at halo masses of  $\sim 10^{10} M_{\odot}$  or lower.

#### 4.2 Reveal the emission from dwarf galaxies with follow-up observations

Constraining the SHMR in the low-mass range requires accurate measurements of the luminosity of galaxies hosted by subhalos. Although detecting the luminous emission of those dwarf galaxies is challenging, our experiments indicate that its effect on subhalo mass measurements might be detectable in Euclid lensing data. This suggests that it is possible to disentangle the satellite galaxy light component through more sophisticated lens modelling. Moreover, if satellite galaxies do not overlap with the lensed arc, their signals will not be obscured by the arc’s emission, and they may even be observed directly. A particularly intriguing example has already been identified: SDSSJ0946+1006, a strong lens system discovered by the Sloan Lens ACS Survey (SLACS; [Bolton et al. 2008](#)), is be-

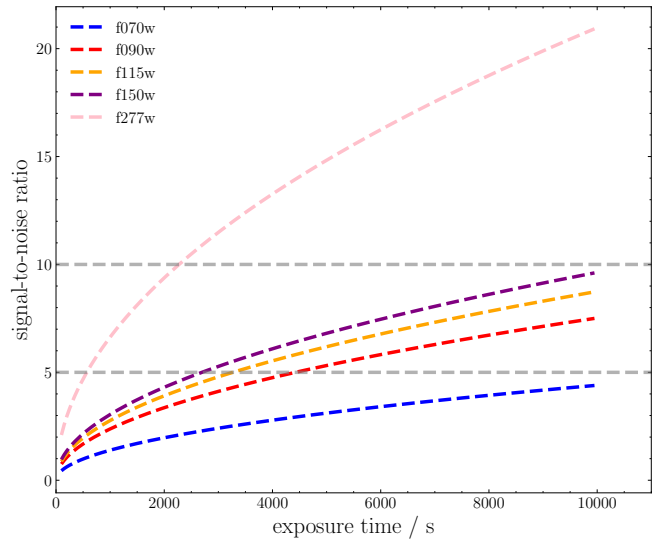


**Figure 8.** The signal-to-noise ratios of the brightest pixel for a  $1 \times 10^8 M_{\odot}$  low surface brightness galaxy as a function of exposure time across different JWST bands. The different bands are represented in various colours.

lieved to host a subhalo with an unusually high concentration ([Minor et al. 2021](#)). One potential explanation for this high concentration is the presence of a galaxy component within the subhalo that was not accounted for in previous studies. The experiments conducted in this work indicate that if this high concentration is due to a satellite galaxy within the subhalo, it is more likely caused by the light contribution from the satellite galaxy rather than its mass contribution. However, no light signals from a satellite galaxy in this system have been observed to date. [Despali et al. \(2024\)](#) analysed analogues of this subhalo in TNG50-1 and found that the luminosities of galaxies in these analogues are  $\geq 2$  orders of magnitude brighter than the  $3\sigma$  upper limit derived from HST observations, suggesting a potential tension with the cold dark matter (CDM) model or small-scale CDM hydrodynamical simulations.

We take SDSSJ0946+1066 as an example to illustrate the potential for directly detecting dwarf galaxies within subhalos. We assume the presence of a dwarf galaxy and simulate the achievable signal-to-noise ratio (SNR) with JWST observations. Based on the results of [Nightingale et al. \(2023\)](#), we hypothesise that the mass of the subhalo is  $1 \times 10^{11} M_{\odot}$ . Considering the various SHMRs presented in [Figure 7](#), we assume that the subhalo hosts a low surface brightness galaxy (LSBG) with a stellar mass of  $1 \times 10^8 M_{\odot}$ , which is approximately the lower mass limit predicted by these SHMRs. Using the SHMR in the SDSS  $r$ ,  $i$ ,  $z$ , and  $J$ ,  $K$  bands from [Du et al. \(2020\)](#), we estimate the stellar mass-to-light ratio  $M_*/L_*$  for a comparable galaxy at redshift  $z = 0.22$  in the JWST bandpasses F070W, F090W, F115W, F150W, and F277W. To ensure a conservative estimate, we adopt the  $3\sigma$  upper bound of the [Du et al. \(2020\)](#) relation, resulting in  $M_*/L_*$  values of 1.86, 1.48, 1.41, 1.58, and 1.07 for these respective filters. Using the Pandeia engine of the Exposure Time Calculator, we estimate the SNR of the brightest pixel across different bands, as shown in [Figure 8](#). With a few hundred seconds of exposure, this dwarf galaxy could be observed visually in F277W. This result demonstrates the possibility that, combined with deep-field observations, we could identify and study a significant number of faint dwarf galaxies associated with subhalos.



### 4.3 Is resolution important?

For the subhalo mass measurement of each individual lens, a detection threshold of an evidence increase ( $\Delta \ln E$ ) greater than 5 ensures an unbiased estimation. This statistical criterion selects models that include a subhalo with a confidence level of  $3.6\sigma$  (Jeffreys 1998). In our idealised mock lens tests, which exclude potential systematics in lens modelling, we consistently recover the subhalo signal using this threshold. However, real lenses may exhibit additional systematics that cannot be accounted for by the lens model, such as unknown complexities in the lens mass distribution. As a result, a threshold of  $\Delta \ln E = 5$  may lead to numerous false-positive subhalo detections, necessitating a more stringent criterion, such as  $\Delta \ln E = 10$  (Nightingale et al. 2023) or  $\Delta \ln E = 50$  (Despali et al. 2024). Moreover, as shown in Figure 7, accurately constraining subhalo properties at the population level requires detections with even higher statistical significance. Unfortunately, Euclid’s resolution may not be sufficient to provide a rich and complete dataset. As discussed in Section 3.1, of the 74 detected subhalos, only 29 exhibit a  $\Delta \ln E > 10$ , and only one exceeds 20. Therefore, it is anticipated that a significant fraction of subhalo candidates observed by Euclid will not be definitively confirmed. The absence of high-confidence subhalo modelling will consequently limit the precision of the constraint on the SHMR. Additionally, subhalos with lower concentrations than the average are more diffuse and have smaller enclosed masses within a given radius. Their perturbations are weaker, leading to smaller Bayesian evidence during modelling. This introduces a potential selection effect, where more diffuse subhalos are undetectable by Euclid, which could bias SHMR measurements.

High-resolution imaging is crucial for resolving these issues. Improved resolution enhances the Bayesian evidence by revealing more details of the lensed arc, which can better highlight substructure perturbations. To demonstrate this, we simulate and fit two images using the model described in Section 2.1: one with Euclid-like resolution and the other with a pixel scale of  $0.05''$  and a PSF FWHM of  $0.09''$ , approximating HST’s values. The fitting procedure follows that outlined in Section 2.3. We then compare the Bayesian evidence between the macro model and the subhalo-included model. The  $\Delta \ln E$  Bayesian evidence for the Euclid-like image is 8.31, while for the high-resolution image, it increases to 20.20. This substantial increase allows even weakly detected candidates to be confidently identified as subhalos. We also present the evidence increase map from the grid search results, shown in Figure 9. It is clear that the evidence for subhalo detection in the Euclid-like image (left panel) is significantly weaker than in the HST-like image (right panel). With deep imaging from JWST, a considerable number of subhalo candidates could be either confirmed or ruled out as false positives, thereby enhancing the robustness of subsequent modelling.

## 5 CONCLUSION

To date, the number of detected low-mass subhalos has remained limited, primarily due to the relatively small number of strong lensing systems—only a few hundred—identified so far. However, this limitation is expected to be overcome in the coming decades with the advent of next-generation space telescopes. Euclid, CSST, and Roman will provide extensive strong lensing catalogues, while JWST will enable deep follow-up observations. These subhalos are crucial for advancing our understanding of dark matter and its co-evolution with galaxies at the low-mass end. In this work, we perform an end-to-end test to determine whether strong lensing systems observed with Euclid can constrain the SHMR for halos with masses

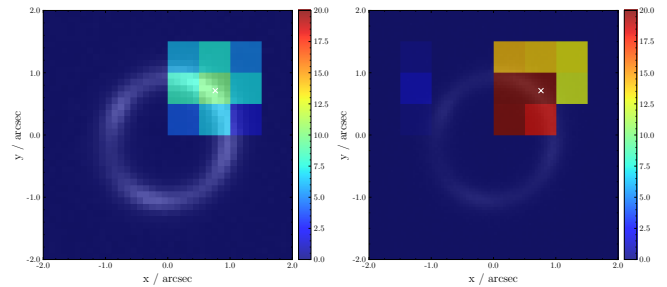


**Figure 9.** Evidence difference maps illustrating the impact of including a subhalo in the lens model for a single lens system at varying image resolutions. The colour bars represent  $\Delta \ln E$ , and the white crosses mark the position of the input subhalo. *Left:* Euclid-like resolution (PSF FWHM =  $0.18''$ , pixel scale =  $0.1''$ ). *Right:* HST-like resolution (PSF FWHM =  $0.09''$ , pixel scale =  $0.05''$ ).

of  $\sim 10^{10} M_{\odot}$ . We simulate images based on a fixed macro model, including a  $3 \times 10^{10} M_{\odot}$  NFW subhalo with varying locations and concentrations, to evaluate whether the mass of the subhalos can be estimated without bias through strong lens modelling. Additionally, we separately include mass or light contributions from a potential satellite galaxy in the subhalo to investigate whether such contamination could lead to biased estimates. Following these tests, we select tens of subhalos and stack their mass estimates to assess whether these measurements can statistically recover the assumed SHMR and quantify the associated uncertainties. Mock images are generated using Euclid VIS specifications, with a signal-to-noise ratio (SNR) of approximately 50 in the brightest pixel. Although this work is based on mock Euclid data, our main conclusions are also applicable to other space telescopes similar to Euclid, such as CSST, which offers comparable performance with the added advantage of providing colour information in the optical band.

(a) Using a detection threshold of  $\Delta \ln E > 5$ , equivalent to a  $3.6\sigma$  significance, we can reliably reconstruct the mass distribution of each individual lens without bias, irrespective of its location. We can likewise model a subhalo whose concentration exceeds the L16 prediction by  $2\sigma$ , again without incurring bias. However, at the population level, subhalo masses inferred from a sample with  $\Delta \ln E > 5$  exhibit a systematic bias: the stacked mass of 85 subhalos underestimates the true  $M_{200}$  by  $1.83\sigma$ . The log-uniform prior partially drives this effect, causing more underestimations than overestimations. Raising the detection threshold to  $\Delta \ln E > 10$  boosts the significance to above  $5\sigma$ , making the posterior distributions more strongly governed by the likelihood than by the priors and thereby yielding accurate and precise population-level mass estimates.

(b) With 48 subhalos detected above the threshold of  $\Delta \ln E > 10$ , we are able to constrain the halo mass for a given stellar mass with a  $1\sigma$  error of 0.0449 dex. Compared to the variance in predictions from previous studies, which is  $\gtrsim 0.5$  dex, subhalos detected via strong lensing are expected to provide precise constraints on the SHMR.

(c) Following the SHMR of Girelli et al. (2020), we assume that the satellite galaxy hosted by a  $\sim 10^{10} M_{\odot}$  subhalo has a stellar mass of  $10^{8.22} M_{\odot}$  and a mass-to-light ratio of  $2 M_{\odot} / L_{\odot}$ . We find that when the mass contribution from the satellite galaxy is included in mock lensing datasets but not properly accounted for in lens modelling, the subhalo mass can still be accurately modelled for both individual lenses and population-level inference. However, the light contribution from the satellite galaxy, although weak, causes the peak of the population-level inference to overestimate  $M_{200}$  by  $\sim 0.5\sigma$ , and the

stacked measurement, using  $\sim 50$  lenses, to overestimate the input  $M_{200}$  by  $5.99\sigma$ . Since a  $\sim 10^{10} M_{\odot}$  subhalo is highly likely to host a dwarf galaxy, the light emission from such a galaxy must be properly accounted for in lens modelling to achieve an unbiased constraint on the SHMR.

We demonstrate that strong lensing is an exceptionally powerful tool for constraining the SHMR at small mass scales ( $M_{\text{halo}} \sim 10^{10}$ ). On one hand, subhalos detected through strong lens modelling are ideal candidates for hosting dwarf galaxies, enabling significant discoveries of such galaxies through follow-up observations. We have shown that a  $10^8 M_{\odot}$  galaxy could be easily detected with the long-wavelength channel of JWST in just a few hundred seconds. Given that subhalos detected by Euclid may not exhibit visible emission, deep follow-up observations will be essential to search for faint halo-galaxy pairs. On the other hand, strong lens modelling allows us to precisely constrain the mass of these subhalos, thereby providing robust constraints on the halo mass for a given stellar mass of the galaxy. By leveraging strong lensing analysis, we can obtain the properties of both subhalos and the galaxies they host, offering a valuable opportunity to further our understanding of the co-evolution of galaxies and dark matter halos.

We also emphasise the importance of high-resolution observations for constraining the SHMR. To achieve precise constraints, high-confidence detections with a  $\Delta \ln E > 10$  are required. However, for a Euclid image, where the signal-to-noise ratio (SNR) of the brightest pixel on the lensed arc is  $\sim 50$ , only 29 out of 161 mock images, with randomly located subhalos, exhibit detection signals with a  $\ln$ -evidence increase  $> 10$ . Increasing the resolution to HST-like values could raise the value of this  $\Delta \ln E$  by  $\sim 10$ , significantly improving the data quality and ensuring a more precise constraint on subhalo properties. Furthermore, higher image resolution may mitigate potential selection effects, where more diffuse subhalos induce weaker perturbations on the image, rendering them undetectable by Euclid and potentially biasing SHMR measurements. In the era of space-based surveys, a vast strong lensing catalog is expected to become available. A combination of wide-field surveys and high-quality follow-up observations will undoubtedly enable us to uncover the physics of the faintest galaxies and their host dark matter subhalos.

## ACKNOWLEDGEMENTS

We acknowledge the support by National Key R&D Program of China No. 2022YFF0503403, the support of National Nature Science Foundation of China (Nos 11988101), the support from the Ministry of Science and Technology of China (Nos. 2020SKA0110100), the science research grants from the China Manned Space Project, CAS Project for Young Scientists in Basic Research (No. YSBR-062), and the support from K.C.Wong Education Foundation. XYC acknowledges the support of the National Natural Science Foundation of China (No. 12303006). This work was performed using the Cambridge Service for Data Driven Discovery (CSD3), part of which is operated by the University of Cambridge Research Computing on behalf of the STFC DiRAC HPC Facility ([www.dirac.ac.uk](http://www.dirac.ac.uk)). The DiRAC component of CSD3 was funded by BEIS capital funding via STFC capital grants ST/P002307/1 and ST/R002452/1 and STFC operations grant ST/R00689X/1. DiRAC is part of the National e-Infrastructure. This work also used the DiRAC@Durham facility managed by the Institute for Computational Cosmology on behalf of the STFC DiRAC HPC Facility ([www.dirac.ac.uk](http://www.dirac.ac.uk)). The equipment was funded by BEIS capital funding via STFC capital grants

ST/P002293/1 and ST/R002371/1, Durham University and STFC operations grant ST/R000832/1. DiRAC is part of the National e-Infrastructure.

## DATA AVAILABILITY

The software used for lens modelling, PyAutoLens, is open source and available at <https://github.com/Jammy2211/PyAutoLens>. Model parameters are available in Table 1. Simulated images and fitting results are available upon request; please contact the authors.

## REFERENCES

- Ade P. A. R., et al., 2016, *Astronomy & Astrophysics*, 594, A13  
 Amorisco N. C., et al., 2021, *Monthly Notices of the Royal Astronomical Society*, 510, 2464–2479  
 Amorisco N. C., et al., 2022, *MNRAS*, 510, 2464  
 Ballard D. J., Enzi W. J. R., Collett T. E., Turner H. C., Smith R. J., 2024, *MNRAS*, 528, 7564  
 Behroozi P. S., Conroy C., Wechsler R. H., 2010, *ApJ*, 717, 379  
 Bolton A. S., Burles S., Koopmans L. V. E., Treu T., Gavazzi R., Moustakas L. A., Wayth R., Schlegel D. J., 2008, *ApJ*, 682, 964  
 Cao X., et al., 2022, *Research in Astronomy and Astrophysics*, 22, 025014  
 Cao X., et al., 2023, CSST Strong Lensing Preparation: Forecast the galaxy-galaxy strong lensing population for the China Space Station Telescope ([arXiv:2312.06239](https://arxiv.org/abs/2312.06239)), <https://arxiv.org/abs/2312.06239>  
 Collaboration E., et al., 2024, Euclid. II. The VIS Instrument ([arXiv:2405.13492](https://arxiv.org/abs/2405.13492)), <https://arxiv.org/abs/2405.13492>  
 Collett T. E., 2015, *ApJ*, 811, 20  
 Despali G., Vegetti S., White S. D., Powell D. M., Stacey H. R., Fassnacht C. D., Rizzo F., Enzi W., 2022, *MNRAS*, 510, 2480  
 Despali G., Heinze F. M., Fassnacht C. D., Vegetti S., Spingola C., Klessen R., 2024, Detecting low-mass haloes with strong gravitational lensing II: constraints on the density profiles of two detected subhaloes ([arXiv:2407.12910](https://arxiv.org/abs/2407.12910)), <https://arxiv.org/abs/2407.12910>  
 Driver S. P., et al., 2022, *MNRAS*, 513, 439  
 Du W., Cheng C., Zheng Z., Wu H., 2020, *AJ*, 159, 138  
 Duffy A. R., Schaye J., Kay S. T., Dalla Vecchia C., 2008, *Monthly Notices of the Royal Astronomical Society: Letters*, 390, L64  
 Engler C., et al., 2020, *Monthly Notices of the Royal Astronomical Society*, 500, 3957–3975  
 Etherington A., et al., 2022, *Monthly Notices of the Royal Astronomical Society*, 517, 3275  
 Etherington A., et al., 2024, *MNRAS*, 531, 3684  
 Euclid Collaboration et al., 2024, *arXiv e-prints*, p. [arXiv:2405.13491](https://arxiv.org/abs/2405.13491)  
 Frenk C., White S., 2012, *Annalen der Physik*, 524, 507–534  
 Girelli G., Pozzetti L., Bolzonella M., Giocoli C., Marulli F., Baldi M., 2020, *Astronomy & Astrophysics*, 634, A135  
 Graham A. W., Erwin P., Trujillo I., Asensio Ramos A., 2003, *AJ*, 125, 2951  
 He Q., et al., 2022a, *MNRAS*, 511, 3046  
 He Q., et al., 2022b, *MNRAS*, 512, 5862  
 He Q., et al., 2023, *Mon. Not. Roy. Astron. Soc.*, 518, 220  
 He Q., et al., 2024, *MNRAS*, 532, 2441  
 Hilbert D., 1891, *Mathematische Annalen*, 38, 459  
 Jeffreys H., 1998, *Theory of Probability*. International series of monographs on physics, Clarendon Press, [https://books.google.com/hk/books?id=\\_PuRmAEACAAJ](https://books.google.com/hk/books?id=_PuRmAEACAAJ)  
 Lange J. U., 2023, *Monthly Notices of the Royal Astronomical Society*, 525, 3181  
 Lange S. C., et al., 2024, *MNRAS*, submitted, 18, 1  
 Li R., Frenk C. S., Cole S., Gao L., Bose S., Hellwing W. A., 2016, *Mon. Not. Roy. Astron. Soc.*, 460, 363  
 Li R., Frenk C. S., Cole S., Wang Q., Gao L., 2017, *Mon. Not. Roy. Astron. Soc.*, 468, 1426

- Ludlow A. D., Bose S., Angulo R. E., Wang L., Hellwing W. A., Navarro J. F., Cole S., Frenk C. S., 2016, *Monthly Notices of the Royal Astronomical Society*, 460, 1214–1232
- Martinet N., et al., 2019, *Astronomy & Astrophysics*, 627, A59
- Minor Q. E., 2024, High detection significance of the dark substructure in gravitational lens SDSSJ0946+1006 is revealed by image pixel supersampling ([arXiv:2408.11090](https://arxiv.org/abs/2408.11090)), <https://arxiv.org/abs/2408.11090>
- Minor Q., Gad-Nasr S., Kaplinghat M., Vegetti S., 2021, *Monthly Notices of the Royal Astronomical Society*, 507, 1662–1683
- Mitchell P. D., Lacey C. G., Baugh C. M., Cole S., 2015, *Monthly Notices of the Royal Astronomical Society*, 456, 1459–1483
- Moster B. P., Naab T., White S. D. M., 2012, *Monthly Notices of the Royal Astronomical Society*, 428, 3121–3138
- Navarro J. F., Frenk C. S., White S. D. M., 1996, *ApJ*, 462, 563
- Nelson D., et al., 2019, *Monthly Notices of the Royal Astronomical Society*, 490, 3234–3261
- Niemiec A., Jullo E., Giocoli C., Limousin M., Jauzac M., 2019, *Monthly Notices of the Royal Astronomical Society*, 487, 653–666
- Niemiec A., Giocoli C., Cohen E., Jauzac M., Jullo E., Limousin M., 2022, *Monthly Notices of the Royal Astronomical Society*, 512, 6021
- Nightingale J. W., Dye S., 2015, *MNRAS*, 452, 2940
- Nightingale J. W., Dye S., Massey R. J., 2018, *Monthly Notices of the Royal Astronomical Society*, 478, 4738–4784
- Nightingale J., et al., 2021, *Journal of Open Source Software*, 6, 2825
- Nightingale J. W., et al., 2023, *Monthly Notices of the Royal Astronomical Society*, 527, 10480
- O’Riordan C. M., Despali G., Vegetti S., Lovell M. R., Moliné Á., 2023, *MNRAS*, 521, 2342
- Pedregosa F., et al., 2011, *Journal of Machine Learning Research*, 12, 2825
- Ritondale E., Auger M. W., Vegetti S., McKean J. P., 2019a, *MNRAS*, 482, 4744
- Ritondale E., Vegetti S., Despali G., Auger M. W., Koopmans L. V. E., McKean J. P., 2019b, *Monthly Notices of the Royal Astronomical Society*, 485, 2179
- Shuntov M., et al., 2022, *Astronomy & Astrophysics*, 664, A61
- Sibson R., 1981, *Interpreting Multivariate Data*. John Wiley and Sons, New York
- Sifón C., Han J., 2024, *Astronomy & Astrophysics*, 686, A163
- Spergel D., et al., 2015, arXiv preprint arXiv:1503.03757
- Suyu S. H., Marshall P. J., Hobson M. P., Blandford R. D., 2006, *MNRAS*, 371, 983
- Taylor E. N., et al., 2011, *MNRAS*, 418, 1587
- Tessore N., Metcalf R. B., 2015, *A&A*, 580, 1
- Vegetti S., Koopmans L. V., 2009, *MNRAS*, 392, 945
- Vegetti S., Koopmans L. V., Bolton A., Treu T., Gavazzi R., 2010, *MNRAS*, 408, 1969
- Vegetti S., Lagattuta D. J., McKean J. P., Auger M. W., Fassnacht C. D., Koopmans L. V., 2012, *Nature*, 481, 341
- Vegetti S., Koopmans L. V. E., Auger M. W., Treu T., Bolton A. S., 2014, *Monthly Notices of the Royal Astronomical Society*, 442, 2017
- Wang J., Bose S., Frenk C., Gao L., Jenkins A., Springel V., White S., 2020, *Nature*, 585, 39
- Zhan H., 2021, *Chinese Science Bulletin*, 66, 1290

This paper has been typeset from a  $\text{\TeX}/\text{\LaTeX}$  file prepared by the author.